Solar Energy Materials & Solar Cells 287 (2025) 113620

Contents lists available at ScienceDirect

Solar Energy Materials and Solar Cells

journal homepage: www.elsevier.com/locate/solmat

Gradient passivating front contact for efficient charge carrier collection in scalable, efficient and stable perovskite solar cells

Hongzhen Su [a,b], Xuesong Lin [c,d], Dezhao Zhang [a,b], Wan Li [a,b], Shuxin Cui [a,b], Yusong Zhou [a,b], Huanpei Huang [a,b], Lin Li [a,b], Li He [a,b], Haotian Zhang [a,b], Hong Liu [a,b], Wenzhong Shen [a,b,e,*]

[a] Institute of Solar Energy and Key Laboratory of Artificial Structures and Quantum Control (Ministry of Education), School of Physics and Astronomy, Shanghai Jiao Tong University, Shanghai, 200240, PR China
[b] Shanghai Non-carbon Energy Conversion and Utilization Institute, Shanghai, 200240, PR China
[c] School of Materials Science and Engineering, Shanghai Jiao Tong University, Shanghai, 200240, PR China
[d] Contemporary Amperex Technology Co. Limited (CATL), Ningde, 352000, PR China
[e] Collaborative Innovation Center of Advanced Microstructures, Nanjing, 210093, PR China

ARTICLE INFO

Keywords:
Perovskite solar cell
Gradient passivating front contact
High efficiency
Stability
Scalability

ABSTRACT

Charge carrier collection is critical for achieving high efficiency and promising stability in perovskite solar cells (PSCs). In this work, we demonstrate a feasible low-temperature-processed gradient passivating front contact (GPFC) between transparent conductive oxide (TCO) and electron transport material, which provides an extra driving force and improved robustness for electron collection. The device based on GPFC strategy achieved a power conversion efficiency of 25.43 % and 24.66 % with an aperture area of 0.09 and 1.00 cm^2, respectively. The GPFC-devices maintained 95.03 % and 91.51 % ± 1.06% of their initial efficiency after enduring 1000 h of thermal stability based on the ISOS-D-2I protocol and 1600 h of operational stability based on the ISOS-L-1I protocol, respectively.

1. Introduction

Perovskite solar cells (PSCs) have emerged as a cutting-edge photovoltaic technology, garnering significant attention due to their rapidly advancing efficiency, which have surpassed 26 % for single-junction devices [1–6]. Despite these remarkable achievements, the efficiency of PSCs is primarily constrained by interface charge carrier losses [3,7–10]. Furthermore, charge accumulation at these interface can lead to irreversible structural and electrical damage, severely compromising the long-term stability of PSCs [11,12]. These interfaces in PSCs could be categorized into two types: (1) heterostructure interfaces between perovskite and charge transport layer (CTLs), which provide a driving force for selective carrier separation; (2) metal (TCO)-semiconductor contacts between CTLs and electrodes, which offer a good Ohmic contact for effective charge carrier collection [13–15]. So far, significant efforts have devoted to passivation of heterostructure interface, encompassing passivation mechanism exploration [16], agent design [17,18] and strategy development [19–24]. However, these passivation strategies exhibit a critical drawback that they fail to enhance the overall performance of PSCs. This may originate from these interlayers between CTL and perovskite primarily improve carrier extraction and transport but have minimal impact on carrier collection efficiency.

In addition to heterostructure interfaces, the design of passivating contact between CTLs and electrodes is expected to play a pivotal role in further improving efficiency and stability of PSCs [25,26]. Passivating contact can extend the carrier diffusion length (L), mitigate the shunt-paths for non-radiative recombination and enhance charge carrier collection, thereby systematically improving the overall device performance including short-circuit current density (J_{SC}), open-circuit voltage (V_{OC}), fill factor (FF) and power conversion efficiency (PCE) [27–29]. These theoretical principles have been successfully demonstrated in silicon solar cells, such as tunnel oxide passivated contact (TOPCon) solar cells and polycrystalline silicon on oxide (POLO) devices, which have achieved efficiencies exceeding 26 % through the implementation

* Corresponding author. Institute of Solar Energy and Key Laboratory of Artificial Structures and Quantum Control (Ministry of Education), School of Physics and Astronomy, Shanghai Jiao Tong University, Shanghai, 200240, PR China.
E-mail address: wzshen@sjtu.edu.cn (W. Shen).

https://doi.org/10.1016/j.solmat.2025.113620
Received 7 February 2025; Received in revised form 28 March 2025; Accepted 29 March 2025
Available online 1 April 2025

of various passivating contacts [30–36]. Moreover, passivating contact can further enhance the interface robustness by lattice matching, thereby extending the operational stability of devices. In PSCs, passivating contact can be categorized into two parts: rear contact at the CTL/rear electrode interface and front contact at transparent conductive oxide (TCO)/CTL interface. Compared to rear counterparts, the passivating front contacts are situated adjacent to depletion zone, which are responsible for assisting the separation of the majority of the photo-generated carriers, directly influencing device performance. However, designing front contacts requires stringent criteria, including suitable energy band alignment at the interface, interface lattice matching, highly optical transparency and superior conductivity [37]. Consequently, developing an effective strategy for passivating front contacts to meet the requirements of PSCs remains a significant challenge.

Herein, we introduce a gradient passivating front contact (GPFC) fabricated through graded n-type doping of hydrolyzed tin oxide with 10 at% and 5 at% antimony (Sb) between fluorine-doped tin oxide (FTO) and SnO_2 nanoparticle (NP) electron transport layer (ETL). Combined with high conductivity, suitable energy band alignment and excellent optical transparency, a best GPFC-device showed an overall performance enhancement and obtain a hysteresis-free performance over 25.43 %, with a V_{OC} of 1.16 V, J_{SC} of 26.03 mA cm^{-2}, and FF of 84.21 %. Furthermore, GPFC based on scalable spray coating process reduces the non-radiative charge recombination in the shunt-paths between perovskite and the TCO. This approach is compatible with substrates exhibiting improved lateral transport properties but larger roughness, facilitating the fabrication of large-area devices. By employing the GPFC strategy, we achieved PSCs with efficiencies of 24.66 % on aperture areas of 1.00 cm^2. Additionally, the homostructure and gradient lattice regulation of FTO/GPFC/SnO_2 NP interface confer outstanding structural and electrical stability. As a result, the GPFC-devices retained 95.03 % and 91.51 % ± 1.06% of their initial efficiency after enduring 1000 h thermal stability under the ISOS-D-2I protocol (unencapsulated PSCs at 65 °C in N_2 atmosphere) and 1600 h of operational stability testing under the ISOS-L-1I protocol (maximum power point tracking (MPPT) of the unencapsulated PSCs at 25 °C in N_2 atmosphere), respectively.

2. Results and discussion

The schematic diagrams of the fluorine-doped tin oxide (FTO)/ETL/perovskite and FTO/GPFC/ETL/perovskite structures are illustrated in Fig. 1a. For the FTO/ETL/perovskite structure, SnO_2 NP struggle to uniformly cover the pyramid tips of the FTO without introducing excessive thickness and additional series resistance (R_S), particularly for the substrate with improved lateral transport properties but higher surface roughness in large-area device. This incomplete coverage leads

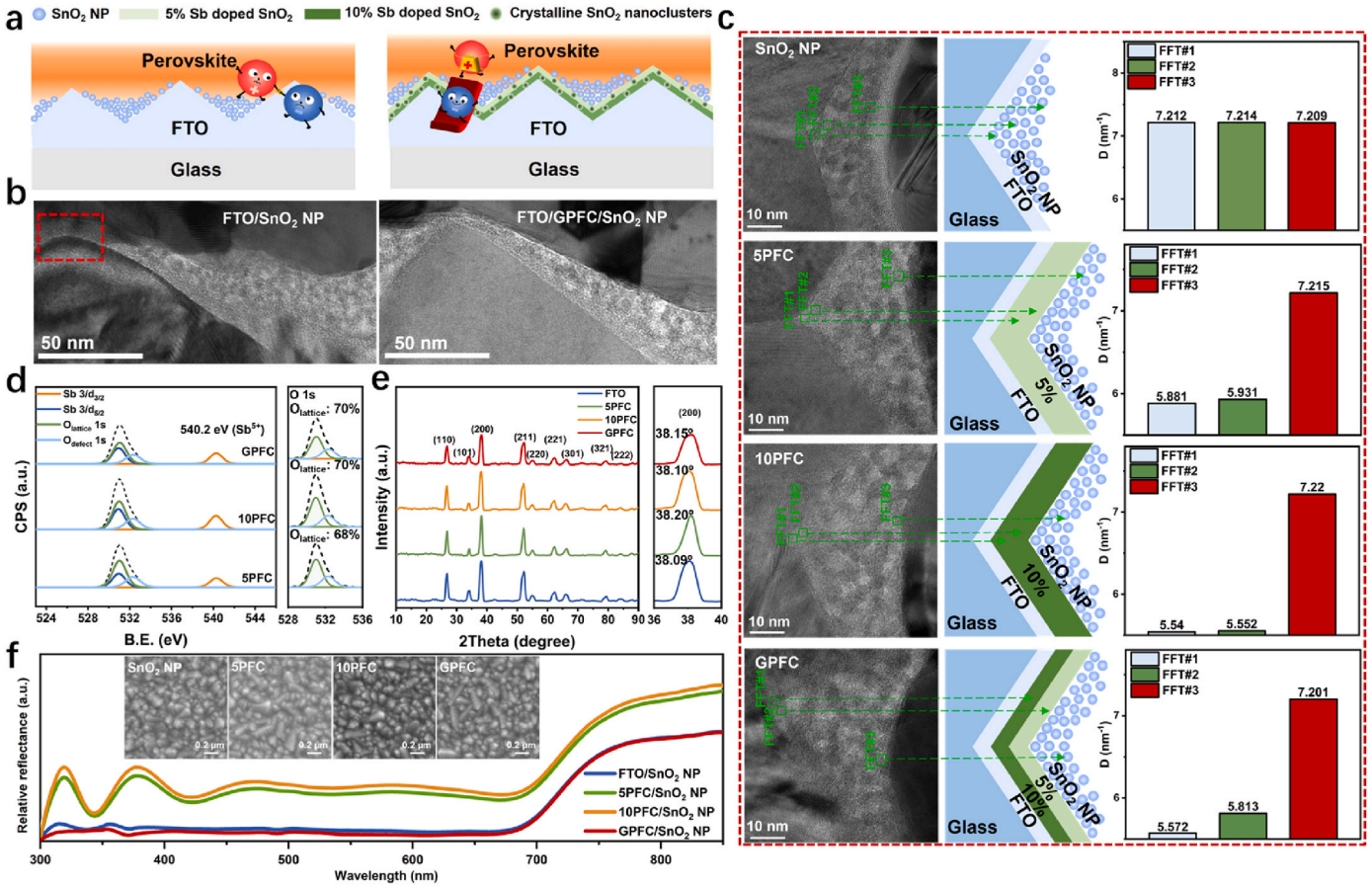

Fig. 1. Formation and characterization of gradient passivating front contacts. (a) Schematic diagrams and (b) cross-sectional TEM images of the FTO/ETL/perovskite and FTO/GPFC/ETL/perovskite structures. (c) Cross-sectional TEM images, the selected area of FFT (green box), structural diagram and bar graph of the FFT diffraction ring diameter for FTO/SnO_2 NP, FTO/5PFC/SnO_2 NP, FTO/10PFC/SnO_2 NP, FTO/GPFC/SnO_2 NP. (d) XPS spectra of Sn 3d and O 1s core level of 5PFC, 10PFC and GPFC atop FTO. The right figure in Fig. 1d shows a zoomed-in view of the O 1s peak. The shaded area, dashed line and solid line represents the $O_{lattice}$ 1s peak, O_{defect} 1s peak and total peak, respectively. The inset value shows the proportion of the peak area occupied by $O_{lattice}$ 1s peak. (e) XRD patterns of FTO, FTO/5PFC, FTO/10PFC and FTO/GPFC. The right figure in Fig. 1e shows a zoomed-in view of the (200) peak. The inset value shows the detailed angle of (200) peak. (f) Relative reflectance and corresponding top-view SEM images (inset) of FTO/SnO_2 NP, FTO/5PFC/SnO_2 NP, FTO/10PFC/SnO_2 NP and FTO/GPFC/SnO_2 NP. (For interpretation of the references to colour in this figure legend, the reader is referred to the Web version of this article.)

to charge recombination at the interface between perovskite and TCO. In contrast, for FTO/GPFC/ETL/perovskite structure, low-temperature-processed hydrolyzed SnO_2 with 10 at% and 5 at% Sb exhibits a "plum pudding" morphology [38], where crystalline SnO_2 nanoclusters are dispersed within a compact amorphous SnO_2 matrix. This structure not only prevents the shunt-paths between FTO and perovskite but also enhances conductivity of GPFC, avoiding the trade-off between compactness and device resistance typically observed in conventional passivation strategies [39]. Additionally, the gradient Sb^{5+} doping in the GPFC induces a built-in electric field perpendicular to the FTO substrate which accelerates electron collection toward the FTO layer and suppresses the electrons-holes recombination [40]. The corresponding cross-sectional transmission electron microscope (TEM) images are shown in Fig. 1b. SnO_2 NP fail to completely cover the textured surface of the FTO substrate, resulting in exposed FTO pyramid tips (as marked by red rectangle), while the GPFC achieves complete coverage of the FTO surface. This prevents direct contact between the perovskite and FTO, thereby reducing non-radiative recombination.

To elucidate the mechanism of passivating front contact with varying doping concentration and structure, we developed three concepts of passivating contacts between FTO and SnO_2 NP ETL: hydrolyzed SnO_2 with 5 % Sb doping (5PFC), hydrolyzed SnO_2 with 10 % Sb doping (10PFC), and gradient hydrolyzed SnO_2 with 10 % and 5 % Sb doping (GPFC). By applying fast fourier transform (FFT) to the cross-sectional TEM images, the diameters of diffraction rings for each passivating contact structures were measured (Fig. S1) and summarized in the bar graph (Fig. 1c). The diameter which is proportional to the lattice constant of SnO_2 nanoclusters in GPFC at 10 % Sb doping layer (FFT#1), 5 % Sb doping layer (FFT#2) and SnO_2 NP layer (FFT#3) are 5.572 nm^{-1}, 5.813 nm^{-1} and 7.201 nm^{-1}. This is originated from the gradient Sb^{5+} doping with larger effective ionic ratio (0.060 nm), compared 0.055 nm of Sn^{4+}. To confirm the Sb doping mechanism in hydrolyzed SnO_2, X-ray photoelectron spectroscopy (XPS) was employed to characterize the valence state of Sb elements. As shown in Fig. 1d, the Sb $3d_{3/2}$ peaks for all samples were located at *ca.* 540.3 eV (540.29 eV for 5PFC, 540.26 eV for 10PFC, and 540.28 eV for GPFC) without a peak around 539.6 eV (Sb^{3+}), indicating n-type doping of Sb^{5+} in hydrolyzed SnO_2. In addition, with the increase of the Sb^{5+} doping concentration, the O defects in SnO_2 are passivated, leading to ratio increase of $O_{lattice}$ in the O elements of SnO_2. Furthermore, depth analysis XPS revealed that the intensity of the Sb $3/d_{3/2}$ peak varies with the depth of SnO_2 and consistent with FFT result (Fig. S2). X-ray diffraction (XRD) results show no additional peak other than those of SnO_2 (Fig. 1e) [41], and characteristic peaks of SnO_2 presented a shift towards low diffraction angle with increasing of Sb^{5+} doping, aligning with FFT results. Hence, the doping mechanism should be related to substitutional Sb^{5+} doping for Sn^{4+} in SnO_2 matrix, as described by **Eq. (1)** to **Eq. (3)**. $SnCl_4{\cdot}5H_2O$ was hydrolyzed to SnO_2 with byproducts of gaseous HCl and H_2O. $SbCl_3$ was hydrolyzed and Sb^{3+} was oxidized to Sb^{5+}. A Sb^{5+} substituted a Sn^{4+} and n-type doped by providing extra free electrons [42]. The relatively low intensity of XRD can be attributed to the "plum pudding" morphology of low-temperature-processed SnO_2 passivating contacts. Furthermore, in Fig. 1e, characteristic peaks of SnO_2 of the 5PFC sample exhibited a narrower full width at half maxima (FWHM) compared to 10PFC sample, likely due to reduces lattice integrity at higher doping concentrations [43]. The broader peak observed for the GPFC sample reflects a combination of 10 % peak and 5 % peak, given the significant depth of X-rays. The optical transparency of substrates plays a critical role in determining the amount of light entering perovskite absorber. As shown in Fig. 1f, top-view SEM images of four FTO/passivating contacts/SnO_2 NP ETL revealed no obvious difference **(insets,** Fig. 1f**)**. However, FTO/GPFC/SnO_2 NP ETL sample presented lowest reflectance (anti-reflection), likely originate from gradient change in refractive index, which enhances light harvesting [44]. Additionally, as shown in Fig. S3, GPFC sample demonstrated the highest transmittance, particularly in the ultraviolet range.

$$2SnCl_4 \cdot 5H_2O \overset{\Delta}{\Rightarrow} 2SnO_2 + 8HCl\uparrow + 6H_2O\uparrow \quad (1)$$

$$2SbCl_3 + 3H_2O + O_2 \overset{\Delta}{\Rightarrow} Sb_2O_5 + 6HCl\uparrow \quad (2)$$

$$Sb_2O_5 \overset{SnO_2}{\Rightarrow} 2Sb_{Sn} + 2e^- + 5O_o \quad (3)$$

The energy band alignment of GPFC was characterized by ultraviolet photoelectron spectroscopy (UPS) and ultraviolet–visible absorption spectroscopy (UV–vis) (Figs. S4 and S5), as shown in Fig. 2a. The fermi level of hydrolyzed SnO_2 shifted toward the conduction band minimum from −4.67 eV to −4.62 eV, with increasing n-type Sb doping (Table S1) [45]. This upshift of the fermi level induced the band bending at the GPFC, reducing the severity of the cliff-like band offset at the GPFC/SnO_2 NP interface. As a result, electron migration toward the FTO layer was accelerated, and electron-hole recombination was suppressed (Fig. 2b) [40]. To investigate the carrier transfer and recombination process, we performed transient photocurrent decay (TPC) and transient photovoltage decay (TPV) measurement (Fig. 2c and d). The TPC and TPV curves were fitted by bi-exponential rate law to obtain charge transport lifetimes (τ_{tr}) and recombination time (τ_{re}), respectively, as summarized in Table S2. A shorter τ_{tr} (0.57 μs) and a prolonged τ_{re} (14.7 μs) of GPFC/SnO_2 NP sample compared with those of SnO_2 NP sample (0.95 μs in TPC and 6.03 μs in TPV), suggesting improved charge carrier extraction and collection, as well as enhanced radiative recombination. The electron mobility (μ) was characterized using space-charge-limited current (SCLC) method, as discussed in Note S1 and shown in Fig. S6. The corresponding results are presented in Fig. 2e. Compared to SnO_2 ETL (275.66 $cm^2\ V^{-1}\ s^{-1}$), the μ of 5PFC/SnO_2 NP, 10PFC/SnO_2 NP, and GPFC/SnO_2 NP increase to 365.38, 329.87 and 401.70 $cm^2\ V^{-1}\ s^{-1}$, respectively. Using the obtained μ in Fig. 2e, the diffusion coefficient was calculated using Eq. (4). and the diffusion length (L) was determined using Eq. (5), as summarized in Table S2. As shown in Fig. 2f, compared with the SnO_2 NP, the carrier diffusion distance for 5PFC sample increased from 1.310 μm to 2.326 μm. Further increasing doping concentration to 10 %, the L decreased to 2.014 μm, likely due to the introduction of additional defects caused by excessive doping. Notably, the GPFC, which combines a "less optimal" 10 % doped layer and an improved 5 % doped layer, achieved a significant enhancement in L to 2.640 μm. Moreover, the carrier collection probability (f_C) was determined by L, as Eq. (6). For a SnO_2 NP ETL thickness of 30 nm, the GPFC improved the f_C at FTO/ETL interface from 97.7 % to 98.9 % (Fig. 2g). The conductive atomic force microscopy (c-AFM) confirmed the improved conductivity of the GPFC (Fig. S7). The average current for 5PFC/SnO_2 NP (1.820 PA), 10PFC/SnO_2 NP(0.905 PA) and GPFC/SnO_2 NP(3.430 PA) was significantly higher than that of the SnO_2 NP (0.406 PA). This trend is consistent with the conductivity measurements obtained from current-voltage curve in Fig. S8.

To further investigating the surface morphology and energy levels of different passivating contact structure, we conduct AFM and KPFM measurements. These properties are closely related to the charge transfer and collection at the interfaces of perovskite/ETL and ETL/TCO, respectively. The surface roughness decreased from 10.03 to 7.52, 7.65 and 7.39 nm for SnO_2 NP to 5PFC/SnO_2 NP, 10PFC/SnO_2 NP and GPFC/SnO_2 NP, respectively (Fig. S9). This reduction in roughness is beneficial for the formation of a compact passivating contact layer. The surface potentials for SnO_2 NP, 5PFC/SnO_2 NP, 10PFC/SnO_2 NP and GPFC/SnO_2 NP were measured to be −151.2, −173.6, −208.3 and −194.1 mV, respectively (Fig. S10). After calibrating the surface potential of the tip with an Au reference (ψ_{Au} = 5.10 eV), the work functions (WFs) of the samples were calculated to be 4.669, 4.646, 4.612 and 4.626 eV, respectively. These values are consistent with the fermi levels measured by UPS (Table S1). The electron transport properties of different passivating contact structure, from perovskite to FTO, were characterized using time-resolved photoluminescence (TRPL) spectroscopy, as

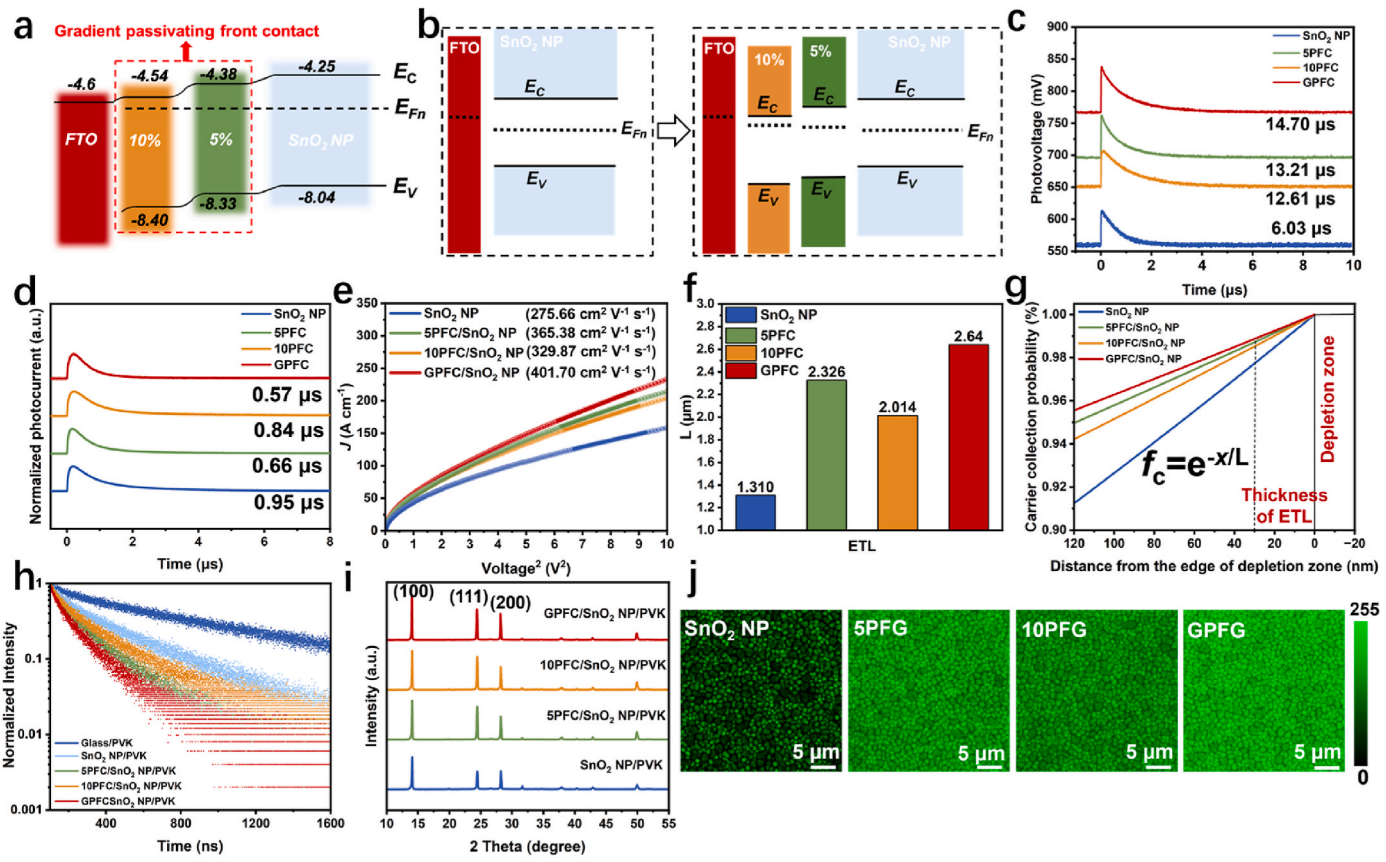

Fig. 2. Charge collection dynamic with gradient passivating front contact. (a) Energy band alignments of GPFC. (b) Schematic illustration of band structure evolution of FTO/GPFC/SnO_2 NP. (c) TPV and (d) TPC measurements for FTO/passivating front contacts/SnO_2 NP/perovskite/C_{60}/Ag. Corresponding (e) carriers diffusing lengths and (f) calculated carrier collection probability. (g) The SCLC curves of the electron-only devices based on SnO_2 NP, 5PFC/SnO_2 NP, 10PFC/SnO_2 NP, GPFC/SnO_2 NP for μ determination. (h) TRPL curves of perovskite atop different substrates. Note that PVK is perovskite. (i) XRD patterns of perovskite atop different substrates. (j) CLSM images of perovskite atop different substrates.

shown in Fig. 2h. The average lifetime (τ_{ave}) of TRPL curves was obtained through bi-exponential fitting and listed in Table S3. The strongest carrier extraction capability was observed in GPFC/SnO_2 NP/perovskite sample, with τ_{ave} of 111.69 ns, which is significantly lower than that of 320.38 ns for the SnO_2 NP/perovskite counterpart.

$$\frac{\mu}{D}=\frac{q}{T\cdot k_B} \tag{4}$$

$$L=\sqrt{D\cdot\tau_{re}} \tag{5}$$

$$f_C=e^{-\frac{x}{L}} \tag{6}$$

here, q denotes the charge of the carrier, and k_B represents the Boltzmann constant.

The influence of different passivating contact structures on the crystallinity and morphology of perovskite was characterized using a combination of SEM images, XRD technique, UV–Vis absorption spectra and confocal laser scanning microscopy (CLSM). As shown in Fig. S11, compared to SnO_2 NPs, the perovskite grains in the 5PFC/SnO_2 NP, 10PFC/SnO_2 NP and GPFC/SnO_2 NP sample exhibited greater uniformity and density, with no observable pinholes. This improvement is attributed to the uniform passivating contact structure, which prevents direct contact between perovskite and FTO [46,47]. The crystallinity of perovskite on the 5PFC/SnO_2 NP, 10PFC/SnO_2 NP and GPFC/SnO_2 NP was improved, as evidenced by the increased absorbance in the UV–Vis region (Fig. 2i and Fig. S12). To further evaluate the PL uniformity of the perovskite layer on different ETLs, CLSM measurements were performed. As shown in Fig. 2j, the perovskite on the GPFC/SnO_2 NP exhibits a more uniform PL intensity compared to the SnO_2 NP counterparts. This uniformity primarily stems from the high homogeneity and reduced defect density, which promoted the uniform nucleation and growth of perovskite [48].

Combined with the induction effect on perovskite growth, the GPFC/SnO_2 NP simultaneously enables efficient electron extraction from perovskite and efficient electron collection at the FTO, thereby achieving a balance in the interface carrier dynamics.

2.1. Device performance

We fabricated PSCs with the following architecture: anti-refection layer/glass/(FTO/GPFC)/SnO_2 NP/perovskite/CsI/n-Octylammonium iodide (OAI)/2,2′,7,7′-tetrakis(*N*,*N*-di-*p*-methoxyphenylamine)-9,9′-spirobifluorene (spiro-OMeTAD)/Au. The cross-sectional SEM image of the PSCs equipped with GPFC/SnO_2 NP is shown in Fig. 3a. Among the three passivating contact structure, the PSCs with GPFC/SnO_2 NP exhibited the largest quasi-fermi level splitting (QFLS) of 1.174 eV, significantly surpassing the results of PSCs with 5PFC/SnO_2 NP (1.162 eV) and 10PFC/SnO_2 NP (1.160 eV), as shown in Fig. 3b (details seen in Note S3). Therefore, the PSC with GPFC/SnO_2 NP was selected (denoted as GPFC-device) to be compared with the SnO_2 NP counterpart (denoted as control-device). The current density-voltage (*J-V*) curves of the champion devices with an aperture area of 0.09 cm^2 are shown in Fig. 3c, with detail parameters listed in Table S4. The GPFC-device obtained an average PCE of 25.43 % with a V_{OC} of 1.16 V, J_{SC} of 26.03 mA cm^{-2} and FF of 84.21 %. In contrast, the champion control-device yielded a lower average PCE of 23.08 %, with a V_{OC} of 1.12 V, J_{SC} of 25.60 mA cm^{-2} and

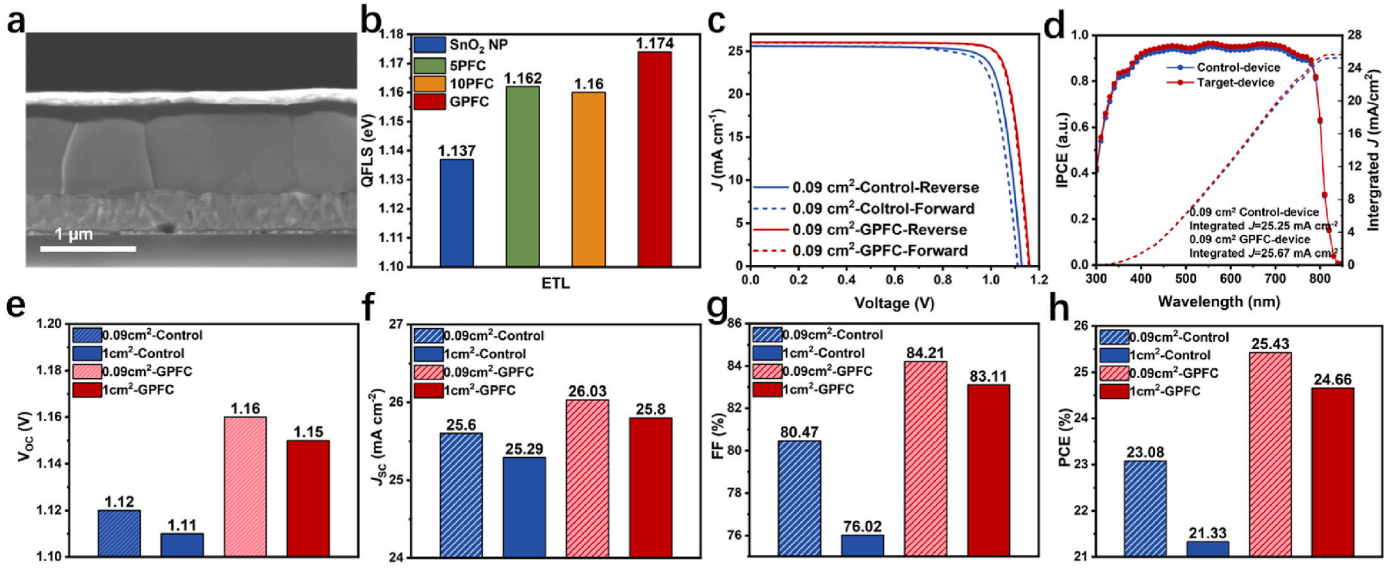

Fig. 3. The efficiency and scalability of GPFC-devices. (a) Cross-sectional images of SEM of GPFC-device. (b) QFLS of PSCs equipped with SnO_2 NP and GPFC/SnO_2 NP. (c) *J-V* curves of champion control and GPFC-devices with an aperture area of 0.09 cm^2. (d) Corresponding IPCE and integrated *J* for the champion control-device and GPFC-device with an aperture area of 0.09 cm^2. (e–g) Relationship between performance parameters and aperture area for the champion control and GPFC-device.

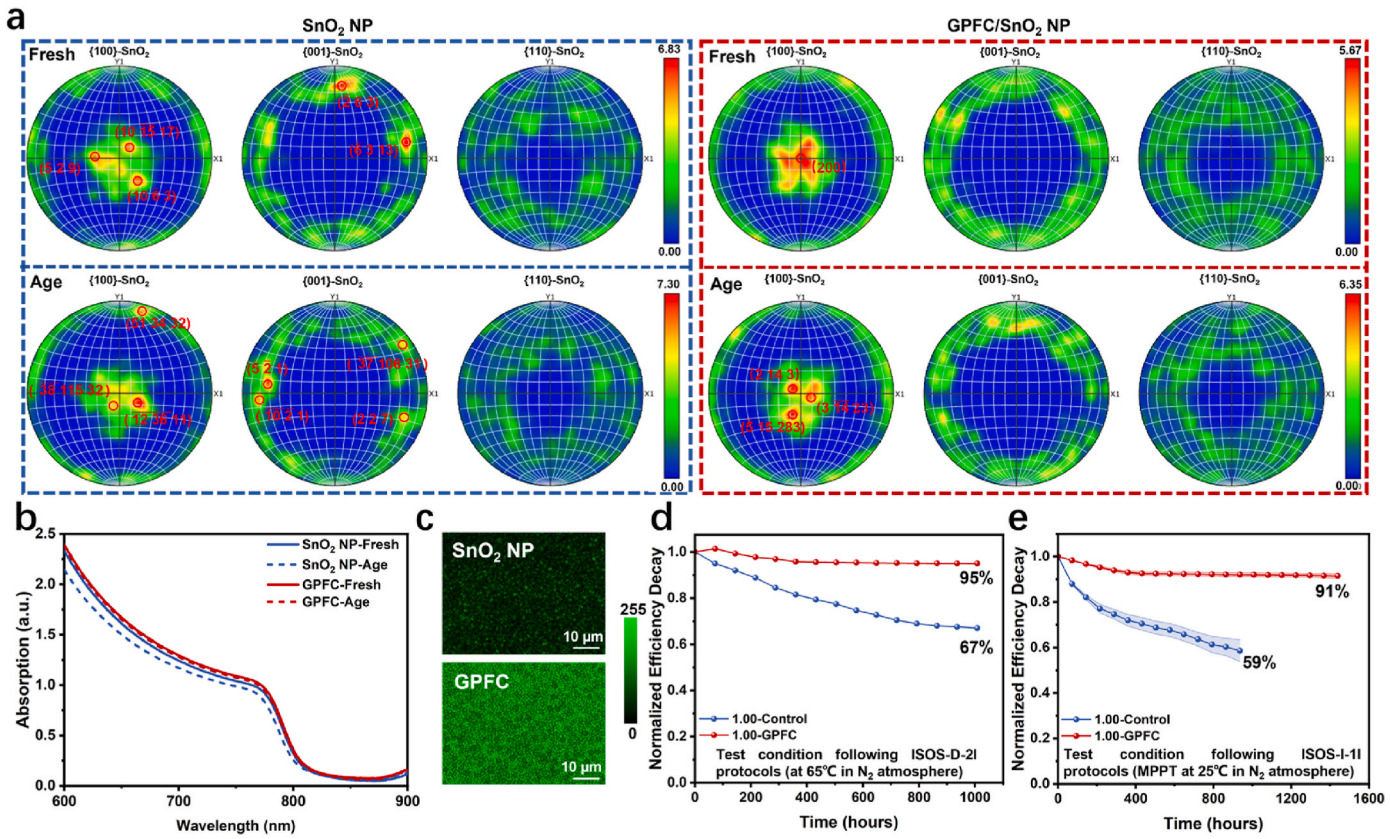

Fig. 4. The stability of GPFC-devices. (a) EBSD images of FTO/SnO_2 NP and FTO/GPFC/SnO_2 with or without undergoing 1000 h heat treatment at 65 °C. (b) UV–vis absorption spectra of FTO/SnO_2 NP and FTO/GPFC/SnO_2 with or without undergoing 720 h of heat treatment at 65 °C. (c) CLSM images of perovskite deposited on FTO/SnO_2 NP and FTO/GPFC/SnO_2 substrates which have undergone 1000 h of heat treatment at 65 °C. (d) Thermal stability of the control and GPFC-devices with an aperture area of 1 cm^2 evaluated under the ISOS-D-2I protocol (unencapsulated PSCs at 65 °C in N_2 atmosphere). The initial PCEs of control and GPFC-devices are shown in Table S5. (e) Operational stability of the control and GPFC-devices across five individual cells with an aperture area of 1 cm^2, tested under the ISOS-L-1I protocol (maximum power point of the unencapsulated PSCs at 25 °C in N_2 atmosphere). The initial PCEs of control and GPFC-devices are shown in Fig. S16, with variations primarily attributed to the replacement of hole transport layers.

FF of 80.47 %. The significant improvement in J_{SC} is primarily attributed to the enhanced of charge carrier collection efficiency [49]. Furthermore, the J_{SC} of the GPFC-device closely matched with the integrated J of 25.67 mA cm^{-2} calculated from the incident photon-to-current efficiency (IPCE) spectrum, with a mismatch of less than 3 % (Fig. 3d).

To evaluate the scalability of the GPFC strategy, we further fabricated the devices with an aperture area of 1.00 cm^2. The *J-V* curves and corresponding performance parameters are shown in Fig. S13 and Table S4. As shown in Fig. 3e–h, the control-device shows a significant efficiency loss from 23.08 % (0.09 cm^2) to 21.33 % (1.00 cm^2), primarily due to the reduction in FF from 80.47 % to 76.02 %. On the contrary, the 1 cm^2 GPFC-device achieved a champion average PCE of 24.66 % with a high FF of 83.11 %. Moreover, the relative efficiency loss (Note S4) for devices with aperture areas from 0.09 to 1.00 cm^2 was reduced from 7.58 % (control-device) to 3.03 % (GPFC-device). This result highlights the superior efficiency and scalability of the GPFC strategy.

Recent studies have demonstrated that the performance degradation of planar PSCs under operational conditions is closely associated with structural and electrical connection failures at the TCO/CTL interface [22,50]. To investigate the influence of GPFC on interface stability of TCO/ETL, FTO/SnO_2 NP and FTO/GPFC/SnO_2 NP were annealed under 65 °C and N_2 atmosphere, simulating device operating conditions. Electron backscatter diffraction (EBSD) was employed for characterizing the crystal orientation changes of SnO_2 before and after heat treatment. As shown in Fig. 4a, the SnO_2 NP prepared on the FTO/GPFC substrate exhibited a predominant crystal orientation near the center of {100} pole diagram. This phenomenon can be attributed to the stronger (200) orientation of the GPFC compared to FTO, which induces the alignment of SnO_2 NPs with the same orientation [51]. Additionally, the adsorption energy of PbI_2 on the high active (200)crystal plane of the SnO_2 NP is greater than that on lower crystal plane, promoting the formation of uniform and dense perovskite layer, as confirmed by SEM images of perovskite (Fig. S11) [52]. Undergoing 1000 h heat treatment at 65 °C, various dispersed crystal orientations such as (5 $\bar{2}$ 1) and (227) appeared on the FTO/SnO_2 NP sample, indicating the FTO/SnO_2 NP interface failure (Fig. 4a, Fig. S14). In contrast, FTO/GPFC/SnO_2 NP sample showed no noticeable crystal distortion, with the orientations still mainly concentrated near the center of the {100} pole diagram. This enhanced stability is attributed to the gradient lattice structure of the GPFC, which releases the interfacial stress between FTO and SnO_2 NP and enhances the structural stability of the interface, as supported by cross-sectional TEM results (Fig. 1c) [53,54]. The UV–Vis absorption spectra and c-AFM images confirmed that the optical performance and conductivity of the FTO/GPFC/SnO_2 NP remained unaffected after heat treatment (Fig. 4b, Fig. S15). The CLSM images of perovskite deposited on the thermal aged FTO/SnO_2 NP and FTO/GPFC/SnO_2 NP substrates are shown in Fig. 4c. The PL intensity of perovskite on the FTO/SnO_2 NP decreased significantly compared to the fresh substrate (Fig. 2j), whereas the PL intensity on the FTO/GPFC/SnO_2 NP substrate remained high and uniform. Thanks to the homostructure and gradient lattice regulation of FTO/GPFC/SnO_2 NP show an improved structural and electrical stability. The GPFC-devices retained 95.03 % and 91.51 % ± 1.06% of their initial efficiency after 1000 h of thermal stability testing under the ISOS-D-2I protocol (unencapsulated PSCs at 65 °C in N_2 atmosphere) and 1600 h of operational stability testing under the ISOS-L-1I protocol (MPPT of the unencapsulated PSCs at 25 °C in N_2 atmosphere), respectively (Fig. 4d and e).

3. Conclusions

In summary, we propose a well-design gradient passivating front contact by graded n-type doping hydrolyzed tin oxide with 10 at% and 5 at% Sb positioned between FTO and SnO_2 NP. This design enhances carrier collection and improves the overall performance of perovskite solar cells (PSCs). By combining high conductivity, suitable energy band alignment and without optical loss, the champion GPFC-device achieved a hysteresis-free performance of 25.43 %, with a V_{OC} of 1.16 V, J_{SC} of 26.03 mA cm^{-2}, and FF of 84.21 %. Furthermore, the GPFC, fabricated using a scalable spray coating process, effectively reduces the non-radiative charge recombination in the shunt-paths between the perovskite and the TCO. The 1.00 cm^2 GPFC-device obtained a PCE of 24.66 %. Owing to the homostructure and gradient lattice regulation of the FTO/GPFC/SnO_2 NP interface, the devices exhibited outstanding structural and electrical stability. Specifically, The GPFC-devices maintained 95.03 % and 91.51 % ± 1.06% of their initial efficiency after 1000 h thermal stability testing under the ISOS-D-2I protocol and 1600 h operational stability testing under the ISOS-L-1I protocol, respectively.

3.1. Experimental section

Materials and Reagents: All the chemicals were purchased from companies without further purification. TCO: FTO substrates were purchased from Advanced Election Technology Co., LTD with a sheet resistance of 10 (Ω/□). ETL: $SnCl_4 \bullet 5H_2O$ (Sigma Aldrich), $SbCl_3$ (Tokyo Chemical Industry), dispersing SnO_2, 15 % in H_2O colloidal dispersion (Alfa Aesar), deionized water (Sigma Aldrich). Perovskite precursor: $CH(NH_2)_2I$ (FAI, 98 %), CH_3NH_3I (MAI, 98 %), CH_3NH_3Cl (MACl, 98 %), PbI_2 (99.99 %) from Tokyo Chemical Industry, dimethyl sulfoxide (DMSO, 99.9 %), dimethylformamide (DMF, 99.8 %), isopropanol (IPA, 99.5 %) from Sigma Aldrich. Passivation layer: OAI (>98 %), CsI (>99 %) from Tokyo Chemical Industry. HTL: spiro-OMeTAD (99.8 %) from Ningbo Borun New Material Technology Co., LTD, Li-TFSI (99.95 %), 4-*tert*-butylpyridine (*t*BP, 96 %), acetonitrile (ACN, 99.8 %), chlorobenzene (CB, 99.8 %) from Sigma Aldrich. polytriarylamines (PTAA, Sigma Aldrich). 4-isopropyl-4′-methyldiphenyliodonium tetrakis(pentafluorophenyl) borate (TPFB, >98 %, Tokyo Chemical Industry). Buffer layer: MoO_3 (99.998 %) from Alfa Aesar. Electrode: Au (99.999 %) from Beijing Dream Material Technology Co., LTD.

Fabrication of anti-reflection layers: The precursor solution, consisting of silicon dioxide nanoparticles and methyl isobutyl ketone, was obtained from Shanghai Juanrou Newtech Co., LTD and then diluted with IPA at a 1:1 ratio (v:v). The diluted solution was spin-coated atop the glass side of FTO substrates at 3000 r.p.m. for 30 s, followed by the thermal annealing process at 120 °C for 2 h to remove the solvent and form the anti-reflection layer.

Preparation of substrates of FTO/passivating front contact: The patterned FTO were prepared by etching with zinc powder and 6M aqueous hydrochloric acid for 15 s. The patterned FTO were sonicated with detergent, deionized water, ethanol, acetone and IPA each for 15 min. The FTO were treated with ultraviolet ozone under dry air for 20 min, and heated to 180 °C for 10 min. A 20 mL IPA solution of 40 mg $SnCl_4 \bullet 5H_2O$ with 1.3 mg $SbCl_3$ (5 %) or 2.6 mg $SbCl_3$ (10 %) was sprayed within 5 min by an air nozzle onto the hot FTO at a distance of about 15 cm. For 10 %/5 % sample, a 10 mL IPA solution of 20 mg $SnCl_4 \bullet 5H_2O$ with 1.3 mg $SbCl_3$ and 10 mL IPA solution of 20 mg $SnCl_4 \bullet 5H_2O$ with 0.65 mg $SbCl_3$ were sprayed successively. After the spraying, the substrates were annealed at 180 °C for 60 min to promote the crystallization of passivating front contacts, and preserved at 120 °C.

Fabrication of PSCs: The FTO/passivating front contact substrates were treated by UV-Ozone for 20 min and cooled down. To prepare the electron transporting material, a SnO_2 nanoparticle dispersion (1:8/5 v/v) was spin-coated on the substrates at 3000 r.p.m. for 30 s, and annealed at 150 °C for 30 min. The above substrates were further treated by UV-Ozone for 20 min to improve the surface wetting, and quickly transferred to the N_2-filled glove box. Then 1.5M of PbI_2 in DMF:DMSO (9:1/*v:v*) was spin-coated on the SnO_2 ETL at 1500 r.p.m. for 40 s, and annealled at 70 °C for 1 min. Then, a solution of FAI:MAI:MACl (90 mg:13 mg:9 mg) dissolved in 1 mL IPA was dynamically spin-coated on PbI_2 films at 1800 r.p.m. for 30 s, followed by annealing for 15 min at 150 °C under ambient atmosphere (30–34 % relative humidity). After being transferred to the N_2-filled glove box and cooled down, a

passivation layer of CsI (5 nm) was deposited by thermal evaporation, and a passivation layer of OAI solution (5 mg in 1 mL IPA) was spin-coated on perovskite at 5000 r.p.m. for 30 s before the HTL deposition. For the spiro-OMeTAD ETL with 72.3 mg spiro-OMeTAD, 17.5 μL Li-TFSI in ACN (520 mg in 1 mL ACN), 28.8 μL *t*BP were dissolved in 1 mL CB and spin-coated atop perovskite film at 3000 r.p.m. for 30 s. For the PTAA ETL for stability tests, 30 mg PTAA HTLs doped with 3 mg TPFB in 1 mL toluene was spin-coated atop perovskite film at 2000 r.p.m. for 30 s. Then, 120 nm Au electrodes were thermally evaporated as anodes using a shadow mask with a substrate cooling system. The 0.09 (0.3 cm × 0.3 cm)and 1.00 cm^2 (1cm × 1 cm) masks were used to define the active areas during measurements.

Characterization of materials and device performance: TEM images were obtained using a Talos F200X G2 system from the USA, and cross-sectional samples were prepared with the FIB technique using a GAIA3 instrument from the Czech Republic. In order to reduce environmental effects and potential damage from the high-energy FIB, a 2-μm carbon (C) layer was deposited on top of the Pt layers. Additionally, a lower FIB voltage of 5 kV was employed to minimize heat-related alterations to the samples. The in-depth analysis of XPS was measured by ESCALAB QXi spectrometer from American. The XPS and UPS data were collected using an AXIS UltraDLD spectrometer equipped with an Al Kα x-ray source manufactured in China. The signals were calibrated using the peaks of the C 1s core level due to its relatively consistent binding energy. The JEOL JSM-7800F Prime field emission SEM from Japan was utilized to examine the morphology of the samples. The reflectance, transmittance and absorption spectra were analyzed through ultraviolet–visible (UV–vis) absorption spectroscopy using the Lamda 950 instrument from China. TPV and TPC decay were measured by a multifunctional electrochemical analysis instrument with a 640 nm laser under a white light bias on samples. The SCLC method was measured using a multifunctional electrochemical analysis instrument (Zahner, Germany). The current-voltage curves were measured with a Keithley 2400 digital source meter under dark. The AFM and KPFM were carried out on MFP-3D (Oxford instrument, USA) to measure the sample roughness and surface potential. The Fastscan Bio AFM system (Bruker, USA) with a Multi75E-G tip was utilized to acquire the c-AFM images. The TRPL were measured on a FLS1000 system (Edinburgh, English), and fitted by the bi-exponential formula (Eq. S(2) and Eq. S(3)) [55]. The XRD patterns were collected using a multifunctional X-ray diffractometer (D8 Advance Da Vinci, Germany) with a scanning range from 3 to 70° at a scanning rate of 0.3° per second. CLSM images of perovskite atop different substrates were tested by TCS SP8 STED 3X (Leica, Germany). A 532 nm laser incident from the top of perovskite, with a penetration depth of approximately 100 nm. The QFLS results were obtained using a photoluminescence quantum yield (PLQY) system (Quantaurus-QY Plus, China), with further analysis details provided in Note S3. The *J-V* characteristics of PSCs were measured under simulated solar illumination of 100 mW cm^{-2}, Air Mass 1.5 Global spectrum using a WXS-155S-10 solar simulator (Wacom Denso) and recorded with a digital source meter. The solar simulator was calibrated using a standard silicon reference cell certified by the Calibration, Standards and Measurement Team at the Research Center for Photovoltaics in AIST, Japan, ensuring a spectral mismatch of less than 3 %. The *J-V* measurements were conducted during forward scan (−0.2–1.2 V) or reverse scan (1.2 to −0.2 V) sweeps. The IPCE spectrum was determined using monochromatic light with an intensity of 1×10^{16} photons cm^{-2}. The EBSD images were collected by a Raman Imaging- SEM hybrid system (RISE-MAGNA, Czech Republic)

Operational stability test of PSCs based on the ISOS-D-2I and ISOS-L-1I protocol: To assess the stability shown in Fig. 4d and e, PTAA was used instead of spiro-OMeTAD to eliminate concerns about the thermal stability of HTLs. In this case, PTAA was doped with TPFB instead of Li-TFSI and *t*BP. The 5-nm MoO_3 buffer layer was inserted between PTAA and Au electrode to reduce the Au migration from electrodes. The thermal stability of the PSCs was evaluated following the ISOS-D-2I protocol, with measurements taken under dark at 65 °C in N_2 atmosphere. The operational stability of the PSCs was evaluated using a solar cell light resistance testing system following the ISOS-L-1I protocol, with measurements taken at the maximum power point under standard one-sun illumination (100 mW cm^{-2}) with 25 °C in N_2 atmosphere. The PCE of the PSCs mentioned above was monitored every 72 h using the reverse *J-V* scan.

CRediT authorship contribution statement

Hongzhen Su: Writing – review & editing, Writing – original draft, Investigation, Formal analysis, Data curation, Conceptualization. **Xuesong Lin:** Writing – review & editing, Formal analysis. **Dezhao Zhang:** Data curation. **Wan Li:** Investigation. **Shuxin Cui:** Investigation. **Yusong Zhou:** Investigation. **Huanpei Huang:** Conceptualization. **Lin Li:** Data curation. **Li He:** Investigation. **Haotian Zhang:** Investigation. **Hong Liu:** Investigation. **Wenzhong Shen:** Writing – review & editing, Conceptualization.

Declaration of competing interest

The authors declare that they have no known competing financial interests or personal relationships that could have appeared to influence the work reported in this paper.

Acknowledgements

This work was supported by the Natural Science Foundation of China (11834011) and Shanghai New Energy Technology Research and Development Project of 24DZ3000900. The authors thank the Center for the Instrumental Analysis Center of Shanghai Jiao Tong University for assistance of the characterizations.

Appendix B. Supplementary data

Supplementary data to this article can be found online at https://doi.org/10.1016/j.solmat.2025.113620.

Data availability

The data that support the findings of this study are available from the corresponding author upon reasonable request.

References

[1] M.A. Green, E.D. Dunlop, M. Yoshita, N. Kopidakis, K. Bothe, G. Siefer, D. Hinken, M. Rauer, J. Hohl-Ebinger, X. Hao, Solar cell efficiency tables (Version 64), Prog. Photovolt. 32 (2024) 425–441.
[2] H. Min, D. Lee, J. Kim, G. Kim, K.S. Lee, J. Kim, M.J. Paik, Y.K. Kim, K.S. Kim, M. G. Kim, T.J. Shin, S.I. Seok, Perovskite solar cells with atomically coherent interlayers on SnO_2 electrodes, Nature 598 (2021) 444–450.
[3] J.J. Yoo, G. Seo, M.R. Chua, T.G. Park, Y.L. Lu, F. Rotermund, Y.K. Kim, C.S. Moon, N.J. Jeon, J.P. Correa-Baena, V. Bulovic, S.S. Shin, M.G. Bawendi, J. Seo, Efficient perovskite solar cells via improved carrier management, Nature 590 (2021) 587–593.
[4] Q. Jiang, Y. Zhao, X.W. Zhang, X.L. Yang, Y. Chen, Z.M. Chu, Q.F. Ye, X.X. Li, Z. G. Yin, J.B. You, Surface passivation of perovskite film for efficient solar cells, Nat. Photonics 13 (2019) 460–466.
[5] Y. Yang, H. Chen, C. Liu, J. Xu, C.Y. Huang, C.D. Malliakas, H.Y. Wan, A.S.R. Bati, Z.W. Wang, R.P. Reynolds, I.W. Gilley, S. Kitade, T.E. Wiggins, S. Zeiske, S. Suragtkhuu, M. Batmunkh, L.X. Chen, B. Chen, M.G. Kanatzidis, E.H. Sargent, Amidination of ligands for chemical and field-effect passivation stabilizes perovskite solar cells, Science 386 (2024) 898–902.
[6] J. Park, J. Kim, H.S. Yun, M.J. Paik, E. Noh, H.J. Mun, M.G. Kim, T.J. Shin, S. I. Seok, Controlled growth of perovskite layers with volatile alkylammonium chlorides, Nature 616 (2023) 724–730.
[7] S. Liu, J. Li, W. Xiao, R. Chen, Z. Sun, Y. Zhang, X. Lei, S. Hu, M. Kober-Czerny, J. Wang, F. Ren, Q. Zhou, H. Raza, Y. Gao, Y. Ji, S. Li, H. Li, L. Qiu, W. Huang, Y. Zhao, B. Xu, Z. Liu, H.J. Snaith, N.-G. Park, W. Chen, Buried interface molecular hybrid for inverted perovskite solar cells, Nature 632 (2024) 536–542.
[8] H. Chen, C. Liu, J. Xu, A. Maxwell, W. Zhou, Y. Yang, Q. Zhou, A.S.R. Bati, H. Wan, Z. Wang, L. Zeng, J. Wang, P. Serles, Y. Liu, S. Teale, Y. Liu, M.I. Saidaminov, M. Li,

N. Rolston, S. Hoogland, T. Filleter, M.G. Kanatzidis, B. Chen, Z. Ning, E. H. Sargent, Improved charge extraction in inverted perovskite solar cells with dual-site-binding ligands, Science 384 (2024) 189–193.
[9] M. Azam, T. Du, Z.Q. Wan, H. Zhao, H.B. Zeng, R.M. Wei, C.J. Brabec, J.S. Luo, C. Y. Jia, Dual functionality of charge extraction and interface passivation by self-assembled monolayers in perovskite solar cells, Energy Environ. Sci. 17 (2024) 6974–7016.
[10] V.S. Katta, M. Waheed, J.H. Kim, Recent advancements in enhancing interfacial charge transport for perovskite solar cells, Sol. RRL 8 (2024) 2300908.
[11] N. Ahn, K. Kwak, M.S. Jang, H. Yoon, B.Y. Lee, J.K. Lee, P.V. Pikhitsa, J. Byun, M. Choi, Trapped charge-driven degradation of perovskite solar cells, Nat. Commun. 7 (2016) 13422.
[12] X.Y. Wang, Y. Zhong, X. Luo, W.P. Sheng, J. Yang, L.C. Tan, Y.W. Chen, Elimination of charge accumulation by a self-assembled cocrystal interlayer for efficient and stable perovskite solar cells, Energy Environ. Sci. 17 (2024) 569–579.
[13] J.L. Tao, N. Ali, K. Chen, Z.X. Huai, Y.S. Sun, G.S. Fu, W.G. Kong, S.P. Yang, Enhanced efficiency in perovskite solar cells by eliminating the electron contact barrier between the metal electrode and electron transport layer, J. Mater. Chem. A 7 (2019) 1349–1355.
[14] Y.R. Guo, Z.Z. Jin, S. Yuan, J.S. Zhao, M.Y. Hao, Y.J. Qin, L.M. Fu, J.P. Zhang, X. C. Ai, Effects of interfacial energy level alignment on carrier dynamics and photovoltaic performance of inverted perovskite solar cells, J. Power Sources 452 (2020) 227845.
[15] Z. Iqbal, F.S. Zu, A. Musiienko, E. Gutierrez-Partida, H. Köbler, T.W. Gries, G. V. Sannino, L. Canil, N. Koch, M. Stolterfoht, D. Neher, M. Pavone, A.B. Muñoz-García, A. Abate, Q. Wang, Interface modification for energy level alignment and charge extraction in $CsPbI_3$ perovskite solar cells, ACS Energy Lett. 8 (2023) 4304–4314.
[16] X. Wang, J. Li, R. Guo, X. Yin, R. Luo, D. Guo, K. Ji, L. Dai, H. Liang, X. Jia, J. Chen, Z. Jia, Z. Shi, S. Liu, Y. Wang, Q. Zhou, T. Wang, G. Pan, P. Mueller-Buschbaum, S. D. Stranks, Y. Hou, Regulating phase homogeneity by self-assembled molecules for enhanced efficiency and stability of inverted perovskite solar cells, Nat. Photonics 18 (2024) 1269–1275.
[17] C. Liu, Y. Yang, H. Chen, J. Xu, A. Liu, A.S.R. Bati, H.H. Zhu, L. Grater, S.S. Hadke, C.Y. Huang, V.K. Sangwan, T. Cai, D. Shin, L.X. Chen, M.C. Hersam, C.A. Mirkin, B. Chen, M.G. Kanatzidis, E.H. Sargent, Bimolecularly passivated interface enables efficient and stable inverted perovskite solar cells, Science 382 (2023) 810–815.
[18] R. Wang, J.J. Xue, K.L. Wang, Z.K. Wang, Y.Q. Luo, D. Fenning, G.W. Xu, S. Nuryyeva, T.Y. Huang, Y.P. Zhao, J.L. Yang, J.H. Zhu, M.H. Wang, S. Tan, I. Yavuz, K.N. Houk, Y. Yang, Constructive molecular configurations for surface-defect passivation of perovskite photovoltaics, Science 366 (2019) 1509–1513.
[19] J. Peng, D. Walter, Y.H. Ren, M. Tebyetekerwa, Y.L. Wu, T. Duong, Q.L. Lin, J.T. Li, T. Lu, M.A. Mahmud, O.L.C. Lem, S.Y. Zhao, W.Z. Liu, Y. Liu, H.P. Shen, L. Li, F. Kremer, H.T. Nguyen, D.Y. Choi, K.J. Weber, K.R. Catchpole, T.P. White, Nanoscale localized contacts for high fill factors in polymer-passivated perovskite solar cells, Science 371 (2021) 390–395.
[20] L. He, H. Su, Z. Li, H. Liu, W. Shen, Multiple function synchronous optimization by PbS quantum dots for highly stable planar perovskite solar cells with efficiency exceeding 23%, Adv. Funct. Mater. 33 (2023) 2213963.
[21] H. Su, X. Lin, Y. Wang, X. Liu, Z. Qin, Q. Shi, Q. Han, Y. Zhang, L. Han, Stable perovskite solar cells with 23.12% efficiency and area over 1 cm^2 by an all-in-one strategy, Sci. China Chem. 65 (2022) 1321–1329.
[22] H. Tang, Z. Shen, Y. Shen, G. Yan, Y. Wang, Q. Han, L. Han, Reinforcing self-assembly of hole transport molecules for stable inverted perovskite solar cells, Science 383 (2024) 1236–1240.
[23] S.M. Park, M. Wei, N. Lempesis, W. Yu, T. Hossain, L. Agosta, V. Carnevali, H. R. Atapattu, P. Serles, F.T. Eickemeyer, H. Shin, M. Vafaie, D. Choi, K. Darabi, E. D. Jung, Y. Yang, D. Bin Kim, S.M. Zakeeruddin, B. Chen, A. Amassian, T. Filleter, M.G. Kanatzidis, K.R. Graham, L. Xiao, U. Rothlisberger, M. Gratzel, E.H. Sargent, Low-loss contacts on textured substrates for inverted perovskite solar cells, Nature 624 (2023) 289–294.
[24] Z. Li, X.L. Sun, X.P. Zheng, B. Li, D.P. Gao, S.F. Zhang, X. Wu, S. Li, J.Q. Gong, J. M. Luther, Z.A. Li, Z.L. Zhu, Stabilized hole-selective layer for high-performance inverted p-i-n perovskite solar cells, Science 382 (2023) 284–289.
[25] H.R. Tan, A. Jain, O. Voznyy, X.Z. Lan, F.P.G. de Arquer, J.Z. Fan, R. Quintero-Bermudez, M.J. Yuan, B. Zhang, Y.C. Zhao, F.J. Fan, P.C. Li, L.N. Quan, Y.B. Zhao, Z.H. Lu, Z.Y. Yang, S. Hoogland, E.H. Sargent, Efficient and stable solution-processed planar perovskite solar cells via contact passivation, Science 355 (2017) 722–726.
[26] J. Cao, B.H. Wu, R.H. Chen, Y.Y.Q. Wu, Y. Hui, B.W. Mao, N.F. Zheng, Efficient, hysteresis-free, and stable perovskite solar cells with ZnO as electron-transport layer: effect of surface passivation, Adv. Mater. 30 (2018) 1705596.
[27] W. Luo, C.C. Wu, D. Wang, Y.Q. Zhang, Z.H. Zhang, X. Qi, N. Zhu, X. Guo, B. Qu, L. X. Xiao, Z.J. Chen, Efficient and stable perovskite solar cell with high open-circuit voltage by dimensional interface modification, Acs Appl. Mater. Inter. 11 (2019) 9149–9155.
[28] Y. Feng, R. Liu, F.M. Li, M.Q. Jin, Q. Du, Y.J. Rong, H.Y. Hu, M.X. Wang, Y. Li, Z. T. Shen, Y. Liu, H.L. Li, C. Chen, A synergistic co-passivation strategy for high-performance perovskite solar cells with large open circuit voltage, J. Mater. Chem. C 10 (2022) 12699–12707.
[29] X. Li, X. Wu, B. Li, Z. Cen, Y. Shang, W. Lian, R. Cao, L. Jia, Z. Li, D. Gao, X. Jiang, T. Chen, Y. Lu, Z. Zhu, S. Yang, Modulating the deep-level defects and charge extraction for efficient perovskite solar cells with high fill factor over 86%, Energy Environ. Sci. 15 (2022) 4813–4822.
[30] X.B. Yang, J.X. Kang, W.Z. Liu, X.H. Zhang, S. De Wolf, Solution-doped polysilicon passivating contacts for silicon solar cells, Acs Appl. Mater. Inter. 13 (2021) 8455–8460.
[31] J. Zhou, X. Su, Q. Huang, Y. Zeng, D. Ma, W. Liu, B. Yan, J. Ye, J. Yang, X. Zhang, H. Jin, Y. Zhao, G. Hou, Corrigendum to "Approaching 23% efficient n-type crystalline silicon solar cells with a silicon oxide-based highly transparent passivating contact", Nano Energy 99 (2022) 107319.
[32] Martin A. Green, Ewan D. Dunlop, M. Yoshita, N. Kopidakis, K. Bothe, G. Siefer, X. Hao, Jessica Y. Jiang, Solar cell efficiency tables (Version 65), Prog. Photovolt. 33 (2024) 3–15.
[33] F.J. Ma, B. Hoex, G.S. Samudra, A.G. Aberle, Modelling and simulation of field-effect surface passivation of crystalline silicon-based solar cells, Enrgy. Proced. 15 (2012) 155–161.
[34] A. Xie, G. Wang, Y. Sun, H. Cai, X. Su, P. Cao, Z. Li, Z. Chen, J. He, P. Gao, Bifacial silicon heterojunction solar cells using transparent-conductive-oxide- and dopant-free electron-selective contacts, Prog. Photovolt. 32 (2024) 664–674.
[35] M.Q. Khokhar, S.Q. Hussain, S. Chowdhury, M.A. Zahid, D.P. Pham, E.C. Cho, J. Yi, Simulated study and surface passivation of lithium fluoride-based electron contact for high-efficiency silicon heterojunction solar cells, ECS J. Solid State Sci. Technol. 11 (2022) 015001.
[36] D. Xu, Q. Bi, K. Li, K. Gao, X. Wang, W. Shi, S. Wang, C. Xing, X. Zhang, X. Yang, High-performance transparent electron-selective contact for crystalline silicon solar cells, Adv. Funct. Mater. 34 (2024) 2407290.
[37] N.G. Saykar, A. Arya, S.K. Mahapatra, A comprehensive review on defect passivation and gradient energy alignment strategies for highly efficient perovskite solar cells, J. Phys. D Appl. Phys. 55 (2022) 043001.
[38] G.M. Hu, W.J. Qin, M.M. Liu, X.X. Ren, X.M. Wu, L.Y. Yang, S.E. Yin, Scalable room-temperature synthesis of plum-pudding-like $Cs_4PbBr_6/CsPbBr_3$ microcrystals exhibiting excellent photoluminescence, J. Mater. Chem. C 7 (2019) 4733–4739.
[39] Q. Luo, Y. Zhang, C.Y. Liu, J.B. Li, N. Wang, H. Lin, Iodide-reduced graphene oxide with dopant-free spiro-OMeTAD for ambient stable and high-efficiency perovskite solar cells, J. Mater. Chem. A 3 (2015) 15996–16004.
[40] T. Wu, C. Zhen, H. Zhu, J. Wu, C. Jia, L. Wang, G. Liu, N.-G. Park, H.-M. Cheng, Gradient Sn-doped heteroepitaxial film of faceted rutile TiO_2 as an electron selective layer for efficient perovskite solar cells, Acs Appl. Mater. Inter. 11 (2019) 19638–19646.
[41] X.Q. Chen, H.Z. Li, W. Chen, Z.X. Mei, A. Azarov, A. Kuznetsov, X.L. Du, Optimized indium-free transparent conductor by Zn and F co-doping into tin oxide, Sol. Energy Mater. Sol. Cell. 278 (2024) 113211.
[42] Q. Cao, Z. Li, J. Han, S. Wang, J. Zhu, H. Tang, X. Li, X. Li, Electron transport bilayer with cascade energy alignment for efficient perovskite solar cells, Sol. RRL 3 (2019) 1900333.
[43] M.D. Zheng, J.M. Ni, F. Liang, M.C. Wang, X.J. Zhao, Effect of annealing temperature on the crystalline structure, growth behaviour and properties of SnO: Sb thin films prepared by radio frequency (RF)-magnetron sputtering, J. Alloys Compd. 663 (2016) 371–378.
[44] C.Y. Fang, Y.L. Liu, Y.C. Lee, H.L. Chen, D.H. Wan, C.C. Yu, Nanoparticle stacks with graded refractive indices enhance the omnidirectional light harvesting of solar cells and the light extraction of light-emitting diodes, Adv. Funct. Mater. 23 (2013) 1412–1421.
[45] X.F. Ling, J.J. Guo, C.X. Shen, Y.P. Li, H.X. Tian, X.B. Yuan, L. Gui, X.L. Zhang, B. Li, S.J. Chen, R. Li, J.Y. Yuan, W.L. Ma, Y.H. Deng, High-throughput deposition of recyclable SnO electrodes toward efficient perovskite solar cells, Small 20 (2024) 2308579.
[46] S.Q. Yu, Z. Xiong, H.T. Zhou, Q. Zhang, Z.H. Wang, F. Ma, Z.H. Qu, Y. Zhao, X. B. Chu, X.W. Zhang, J.B. You, Homogenized NiOx nanoparticles for improved hole transport in inverted perovskite solar cells, Science 382 (2023) 1399–1404.
[47] H. Bi, X. Zuo, B.B. Liu, D.M. He, L. Bai, W.Q. Wang, X. Li, Z.Y. Xiao, K. Sun, Q. L. Song, Z.G. Zang, J.Z. Chen, Multifunctional organic ammonium salt-modified SnO nanoparticles toward efficient and stable planar perovskite solar cells, J. Mater. Chem. A 9 (2021) 3940–3951.
[48] P. Barua, I. Hwang, Bulk perovskite crystal properties determined by heterogeneous nucleation and growth, Materials 16 (2023) 16052110.
[49] J. Nelson, The Physics of Solar Cells, Imperial College Press, 2005.
[50] D.L. Zhang, H.M. Tian, S.X. Bu, T.T. Yan, J.F. Ge, T. Lei, W.G. Bi, L.K. Huang, Z. Y. Ge, Efficient planar heterojunction perovskite solar cells with enhanced FTO/SnO_2 interface electronic coupling, J. Alloys Compd. 831 (2020) 154717.
[51] W.S. Kim, D. Kim, K.J. Choi, J.G. Park, S.H. Hong, Epitaxial directional growth of tin oxide (101) nanowires on titania (101) substrate, Cryst. Growth Des. 10 (2010) 4746–4751.
[52] Y. Yang, L. Yang, S. Feng, Y. Niu, X. Li, L. Cheng, L. Li, W. Qin, T. Wang, Q. Xu, H. Dong, H. Lu, T. Qin, W. Huang, Active SnO_2 crystal planes enable efficient and ultra-bendable n-i-p perovskite solar cells with record certificated power conversion efficiency, Adv. Energy Mater. 13 (2023) 2300661.
[53] G.T. Duan, K. Zhang, W.F. Zhang, H. Shu, Y.G. Yang, X.Q. Zhou, C.J. Liu, L. Yu, X. Yu, Y.L. Huang, X.J. Wu, C.T. Peng, S.F. Yang, M. Liang, W.H. Zhang, H.R. Tan, Fabricate the compressive-strained perovskite solar cells through the lattice-matching chelation, ACS Energy Lett. 8 (2023) 2308–2315.
[54] C. Luo, G.H.J. Zheng, F. Gao, X.J. Wang, C.L. Zhan, X.Y. Gao, Q. Zhao, Engineering the buried interface in perovskite solar cells via lattice-matched electron transport layer, Nat. Photonics 17 (2023) 856–864.
[55] X.S. Lin, H.Z. Su, S.F. He, Y.A. Song, Y.B. Wang, Z.Z. Qin, Y.Z. Wu, X.D. Yang, Q. F. Han, J.F. Fang, Y.Q. Zhang, H. Segawa, M. Grätzel, L.Y. Han, In situ growth of graphene on both sides of a Cu–Ni alloy electrode for perovskite solar cells with improved stability, Nat. Energy 7 (2022) 520–527.